A numerical study of stress variability in heterogeneous fractured rocks

Qinghua Lei[a], Ke Gao[b],*

[a] Department of Earth Sciences, ETH Zürich, Zürich, Switzerland
[b] Geophysics Group, Los Alamos National Laboratory, Los Alamos, USA

ARTICLE INFO

ABSTRACT

We conduct numerical simulations to investigate the variability of local stresses in heterogeneous fractured rocks subjected to different far-field stress conditions. A realistic fracture network is constructed based on a real outcrop mapped at the Hornelen Basin in Norway. The heterogeneity of the rock material is modelled using a Weibull distribution of Young's modulus characterised by a homogeneity index m. As m decreases, the rock material becomes less homogeneous. The distribution of local stresses in the fractured rock under far-field stress loading is derived from a hybrid finite-discrete element model, and the stress variability is further analysed using a tensor-based formalism that faithfully honours the tensorial nature of stress data. The local stress perturbation is quantified using the Euclidean distance of each local stress tensor to the mean stress tensor, and the overall stress dispersion is measured using the effective variance of the entire stress tensor field. We show that the local stress field is significantly perturbed when the far-field stresses are associated with a high stress ratio and imposed at a critical direction in favour of intense sliding along preferentially-oriented fractures. The strong correlation between fracture sliding and local stress variability are further revealed from a scanline sampling analysis through the domain. Furthermore, larger perturbation of local stresses can be induced as the inhomogeneity of the rock materials increases (i.e. m decreases). Whether the stress field is dominated by fractures or matrix depends on the far-field stress state, material inhomogeneity, and fracture properties. If the rock material is highly heterogeneous, stress variability is controlled by the matrix when the far-field stress ratio is low; however, the stress distribution becomes more affected by fractures as the stress ratio increases. If the rock material is more homogeneous, the system tends to be more dominated by fractures even under a relatively low stress ratio.

1. Introduction

The state of in-situ stress in fractured rocks is governed by tectonic stresses and local perturbations.[1] The tectonic (or far-field) stresses related to plate-driving forces are typically uniform over the lithospheric scale,[2] while local perturbations induced by topography, discontinuity, material inhomogeneity, and anisotropy as well as engineering processes have much smaller wavelengths.[3] The superimposition of the two categories of forces leads to spatially variable in-situ stress state. Many studies have been conducted to investigate the effects of discontinuities (e.g. faults and joints) on perturbing the regionally uniform tectonic stress field.[4–9] However, much less efforts have been devoted to understanding the impact of material inhomogeneity (e.g. rock modulus) on stress variability in fractured rocks. Furthermore, the potentially interactive roles of different controlling factors (e.g. far-field stress state, fracture network, and material inhomogeneity) in developing local stress variability need to be better understood. Thus, in this paper, we explore these problems in detail by employing the state-of-the-art numerical simulation combined with a novel tensor-based stress analysis method.

In the past decades, different numerical methods have been developed to simulate the geomechanical behaviour of rock masses embedded with pre-existing fractures, such as the finite difference method,[10,11] the discrete element method,[12] the bonded-particle method,[13] and the hybrid finite-discrete element method (FEMDEM).[14,15] Many important and realistic geomechanical characteristics of fractured rocks under far-field stresses including rock deformation, block rotation, fracture displacement and crack propagation were well captured. Furthermore, many numerical techniques have also been used to model the deformation and strength behaviour of heterogeneous intact rocks, such as the finite element method,[16–18] the smoothed particle hydrodynamics method,[19] the local degradation method,[20,21] and the discrete element method.[22–24] The inhomogeneous nature of rock materials was considered either explicitly using a Voronoi-based microstructural representation[24] or

* Corresponding author.
    E-mail address: kegao@lanl.gov (K. Gao).

implicitly as the variation of material properties following a Weibull distribution.[25] Here, we integrate the Weibull distribution model into the FEMDEM approach to simulate the complex geomechanical behaviour of heterogeneous fractured rocks, including the stress/strain of heterogeneous matrix, the mechanical interaction of discrete blocks, the nonlinear deformation of pre-existing fractures, and the propagation of new cracks driven by stress concentrations. By further employing the recently developed tensor-based formalism for stress variability characterisation,[9,26] we aim to explore how far-field stress, fracture distribution, and material inhomogeneity act interactively to engender local stress perturbation in geological media, and to gain insights into the physical mechanisms that govern stress variability.

In this study, we focus on the two-dimensional (2D) scenario, which is applicable for a sedimentary formation whose lateral characteristic scale is much larger than its transversal one. We assume that the in-situ stress field in the fractured rock develops entirely based on the imposed contemporary tectonic stresses, whereas the possible residual stress effect is not considered. The rest of the paper is organised as follows. In Section 2, a natural fracture network model based on a real outcrop is constructed, and the numerical method for geomechanical modelling of heterogeneous fractured rocks is described. In Section 3, the results of stress calculation and analysis are shown. Finally, a discussion is given and conclusions are drawn.

2. Methodology

The fracture network used in this research is based on a 18 m × 18 m outcrop map (Fig. 1a) of a Devonian age sandstone located at the Hornelen Basin, western Norway.[27] This fracture pattern consists of more than 2000 joints, which are mostly perpendicular to the bedding. Three major joint sets are identifiable with their mean set orientations as 5°, 50° and 120° (Fig. 1b-d), with respect to the x-axis of the selected local coordinate system (Fig. 1a). It can be seen that the 120° set has the largest number of fractures, and the 5° set has the longest average fracture length. The formation of this fracture system

was interpreted as the result of the stress release on uplift and erosion.[27]

The geomechanical behaviour of the fractured sandstone under far-field stresses is modelled using a hybrid finite-discrete element method (FEMDEM).[28,29] The FEMDEM model represents a 2D fractured rock using a fully discontinuous mesh of three-node triangular finite elements, which are linked by four-node joint elements (Fig. 2). There are two types of joint elements: unbroken joint elements inside the matrix and broken joint elements along fractures. The deformation of the bulk material is captured by the linear-elastic constant-strain triangular finite elements with the impenetrability enforced by a penalty function and the continuity constrained by bonding forces of unbroken joint elements. The interaction of discrete matrix bodies is calculated based on the penetration of finite elements via broken joint elements. The joint elements (either broken or unbroken) are created and embedded between the edges of triangular element pairs before the numerical simulation and no remeshing is performed during later computation. The FEMDEM model also provides a natural solution to mimicking elasto-plastic fracturing processes in brittle/quasi-brittle materials based on fracture mechanics principles, so that unrealistic high stress concentrations at fracture tips encountered in the conventional finite element analysis can be eliminated.

In the FEMDEM model, the motion of finite elements is governed by the forces acting on the elemental nodes[28]:

$$\mathbf{M}\ddot{\mathbf{x}} + \mathbf{f}_{int} = \mathbf{f}_{ext}, \qquad (1)$$

where $\mathbf{M}$ is the lumped nodal mass matrix, $\mathbf{x}$ is the vector of nodal displacements, $\mathbf{f}_{int}$ are the internal nodal forces induced by the deformation of triangular elements, $\mathbf{f}_{ext}$ are the external nodal forces including external loads $\mathbf{f}_l$ contributed by boundary conditions and body forces, cohesive bonding forces $\mathbf{f}_b$ caused by the deformation of unbroken joint elements, and contact forces $\mathbf{f}_c$ generated by the contact interaction via broken joint elements. The equations of motion are solved by an explicit time integration scheme based on the forward Euler method. The FEMDEM model has been verified[9] against the Westergaard analytical solutions[30] for computing the stress distribution
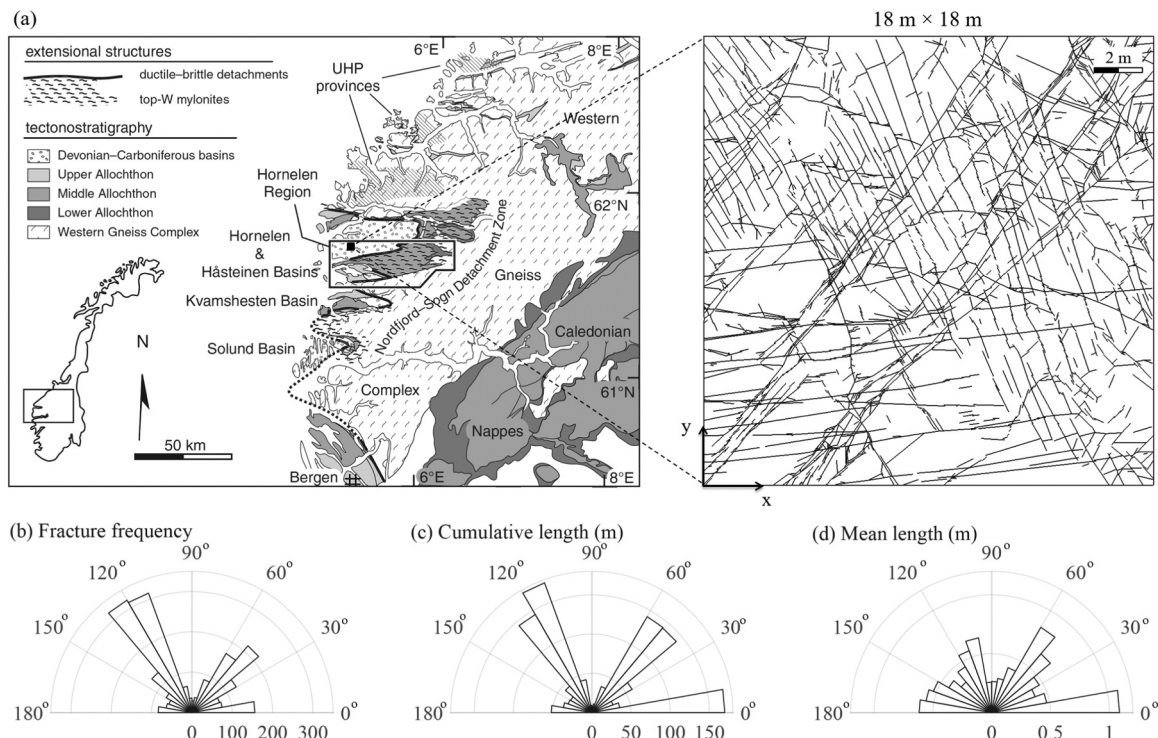

Fig. 1. (a) A 18 m × 18 m outcrop map of the natural fracture system in the Devonian sandstone at Hornelen Basin, western Norway.[27] Rose diagrams illustrating the directional distribution of (b) fracture frequency, (c) cumulative length, and (d) mean length.
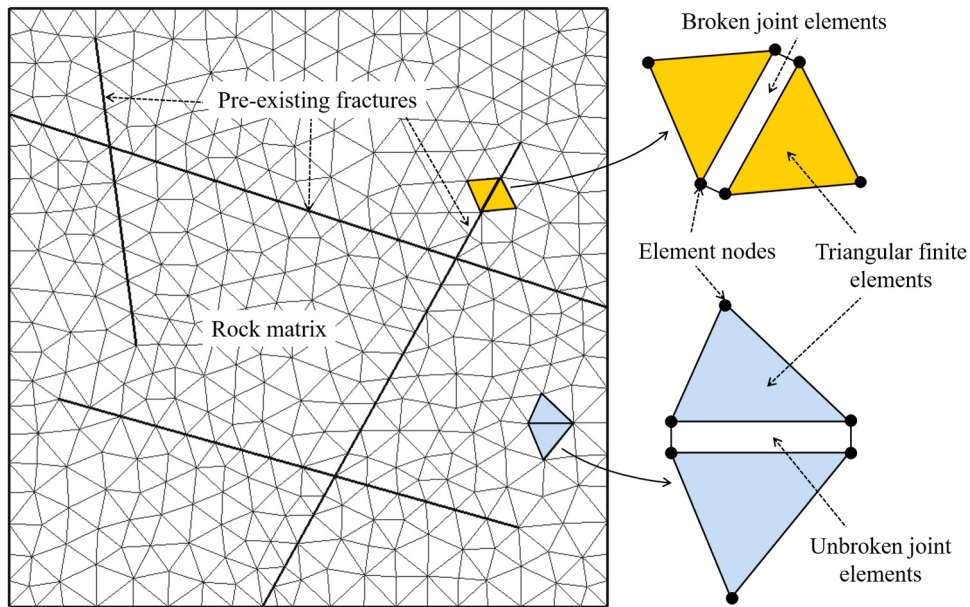
Fig. 2. Representation of a 2D fractured rock using an unstructured, fully-discontinuous mesh of three-node triangular finite elements linked by four-node joint elements.
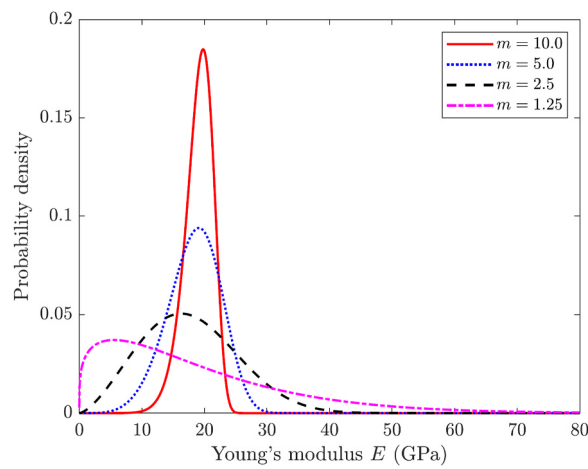

Fig. 3. Variability of Young's modulus in the sandstone formation characterised by the Weibull distribution with different values of shape parameter *m* (or material homogeneity index).
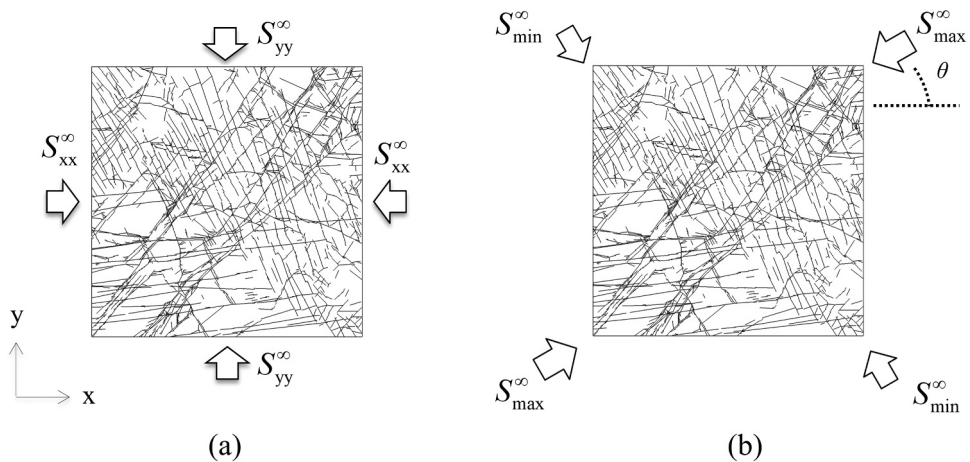

Fig. 4. Application of the far-field stresses (a) orthogonally or (b) obliquely to the problem domain.
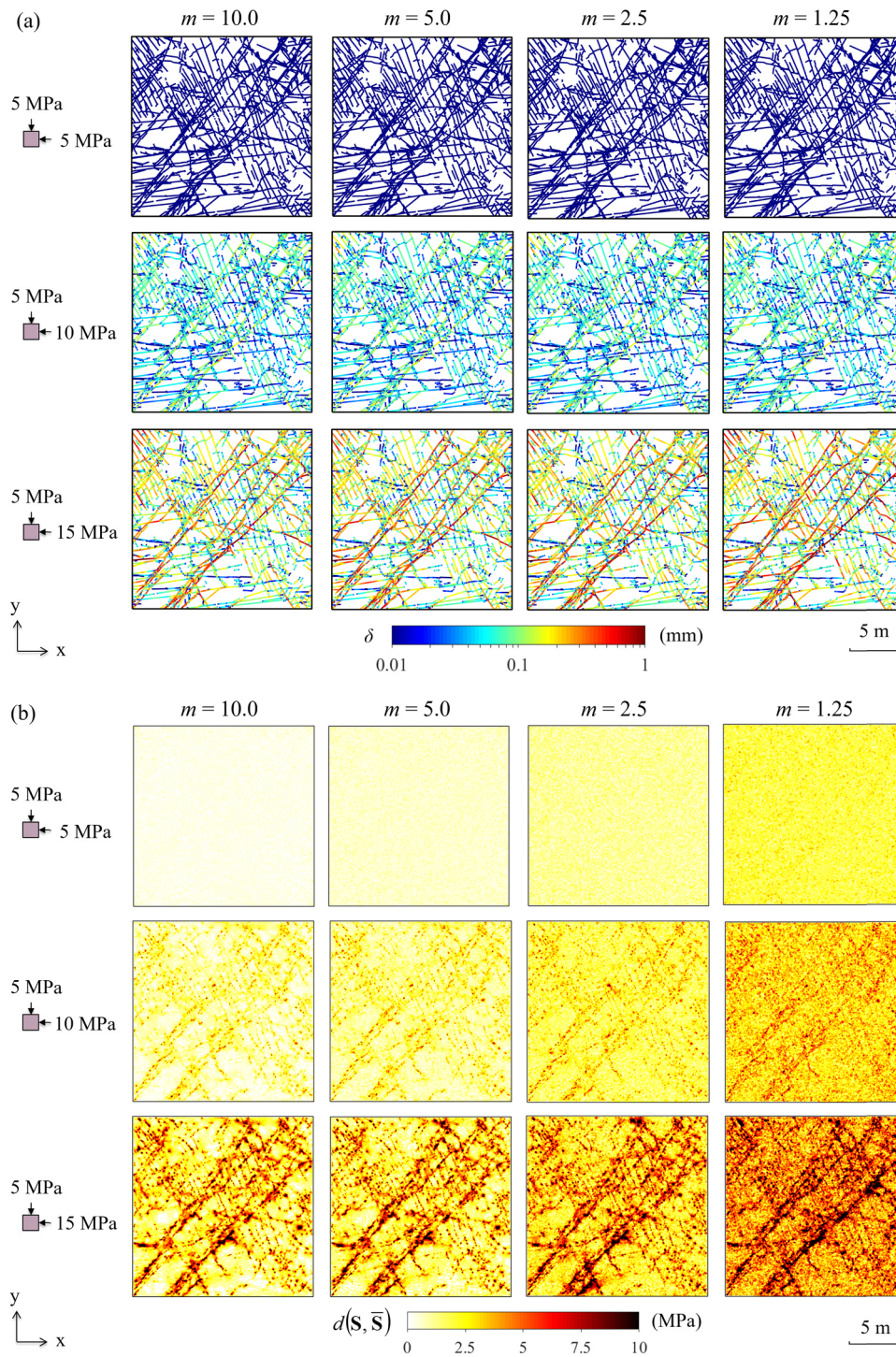
Fig. 5. Distributions of (a) shear displacement δ and (b) local stress perturbation $d(\mathbf{S}, \bar{\mathbf{S}})$ in the heterogeneous fractured rock under different far-field stress ratio conditions.

around a single fracture with a unit half-length and a zero friction coefficient in rock under isotropic remote tension or pure remote shear of unit magnitude.

The material properties of the fractured sandstone are assumed as follows[31,32]: the bulk density is 2500 kg/m^3, the mean Young's modulus is 20.0 GPa, the Poisson's ratio is 0.25, the internal friction coefficient is 1.0, the tensile strength is 20.0 MPa, the internal cohesive strength is 40.0 MPa, and the mode I and II energy release rates are 396.1 and 495.1 J/m^2, respectively. The shear strength of fractures obeys the Coulomb criterion such that frictional sliding occurs if the shear stress

exceeds the product of the effective normal stress and an assumed friction coefficient of 0.85.[32] The complex variation of friction coefficient during fracture shearing[33] is not considered. The variability of Young's modulus of the sandstone is characterised using the Weibull distribution (Fig. 3), and the probability density function is given as[16,34]:

$$f(E) = \frac{m}{\bar{E}}\left(\frac{E}{\bar{E}}\right)^{m-1} \exp\left[-\left(\frac{E}{\bar{E}}\right)^m\right], \tag{2}$$
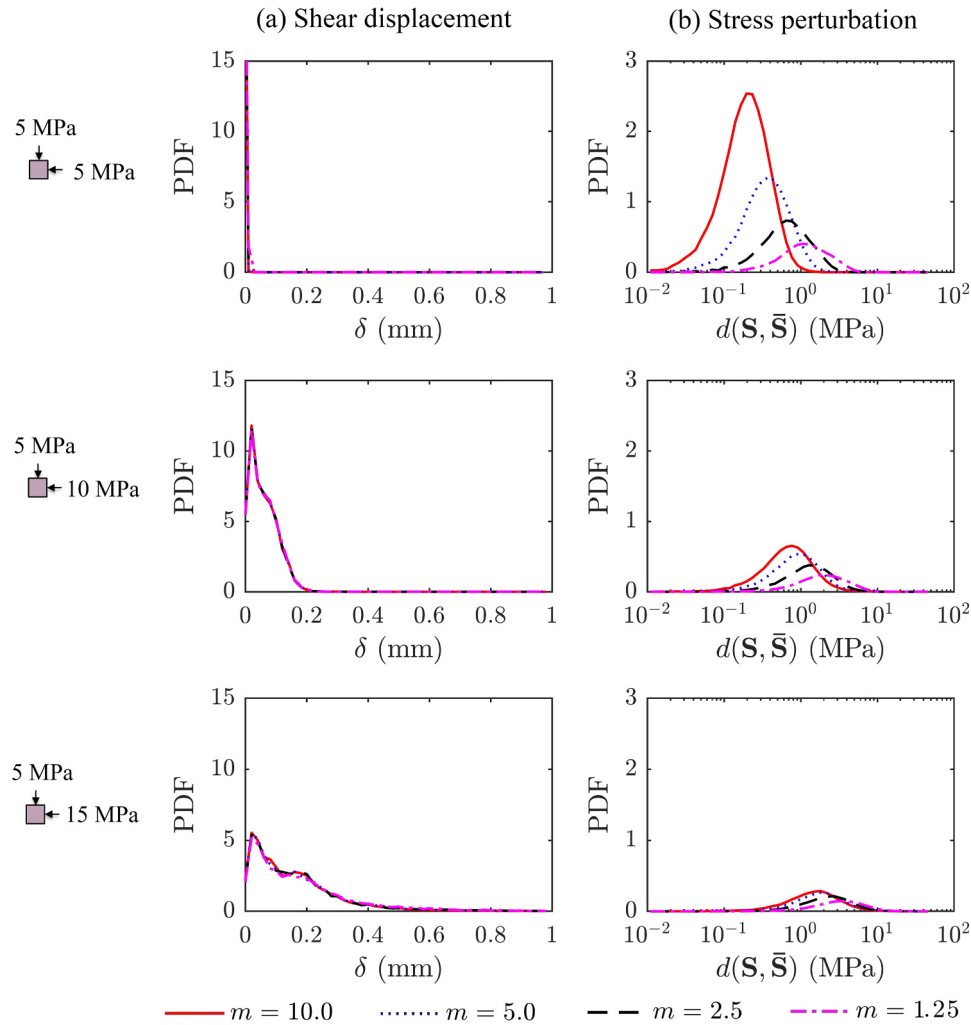
Fig. 6. Probability density functions (PDFs) of (a) shear displacement δ and (b) local stress perturbation $d(\mathbf{S}, \bar{\mathbf{S}})$ in the heterogeneous fractured rock under different far-field stress ratio conditions.

where E is the elemental Young's modulus, $\bar{E}$ is the mean Young's modulus, m is the shape parameter or material homogeneity index. Here, the Weibull distribution is adopted for the purpose of exploring generic scenarios with different degrees of material heterogeneity. The smaller m is, the more heterogeneous the rock is. We represent the spatial variability of E in an element-wise way[16–18] such that E represents the bulk modulus of the rock in each elemental area. If the total number of stochastic E values (i.e. corresponding to the total number of finite elements) is sufficiently large, the potential effect of random number generation may be statistically minor. We consider four different material inhomogeneity scenarios: $m = 1.25$, 2.5, 5.0, and 10.0, covering the conditions from highly heterogeneous to very homogeneous (Fig. 3). It is worth mentioning that other material properties such as Poisson's ratio, tensile strength and cohesion may also be variable in actual rocks, but only the variation of Young' modulus is considered here due to its much more dominant role in redistributing stresses in rock compared to these other properties.[35]

The heterogeneous sandstone containing distributed fractures is discretised using an unstructured mesh with an average element size of 0.075 m ($> 100{,}000$ elements in total). This element size is carefully chosen through a series of mesh sensitivity analyses by considering the accuracy of results and the computational expense (see Appendix B). We impose two sets of far-field stress loading conditions. First, effective far-field principal stresses are loaded orthogonally to the problem

domain (Fig. 4a), and we consider three different stress ratios: (i) S_{xx}^{∞} = 5.0 MPa, S_{yy}^{∞} = 5.0 MPa, (ii) S_{xx}^{∞} = 10.0 MPa, S_{yy}^{∞} = 5.0 MPa, and (iii) S_{xx}^{∞} = 15.0 MPa, S_{yy}^{∞} = 5.0 MPa, corresponding to $S_{xx}^{\infty}/S_{yy}^{\infty}$ = 1.0, 2.0, and 3.0, respectively. Second, effective far-field principal stresses S_{max}^{∞} = 15.0 MPa, S_{min}^{∞} = 5.0 MPa are loaded from different angles ($\theta = 0°$, 10°, 20°, …, 170°) to the fractured rock, as shown in Fig. 4b.

We extract the data of stress distribution from the geomechanical simulation in which all components of the second-rank Cauchy stress tensor at each element are derived. Then we analyse the stress data using the recently developed tensor-based statistical formulation that faithfully honours the tensorial nature of stress[26,36]: We characterise the local stress perturbation using the Euclidean distance between each local stress tensor and far-field stress tensor, $d(\mathbf{S}, \bar{\mathbf{S}})$. We evaluate the overall stress variability in the heterogeneous fractured rocks using the effective variance of the entire stress field, $V_e(\mathbf{S})$. The tensor-based stress analysis method and the mathematical definitions of $d(\mathbf{S}, \bar{\mathbf{S}})$ and $V_e(\mathbf{S})$ are given in Appendix A. A detailed justification of the tensor-based stress variability characterisation method can be found in the previous work.[37,38]

3. Results

Fig. 5 shows the distributions of fracture shear displacement δ and local stress perturbation $d(\mathbf{S}, \bar{\mathbf{S}})$ in the fractured rock associated with
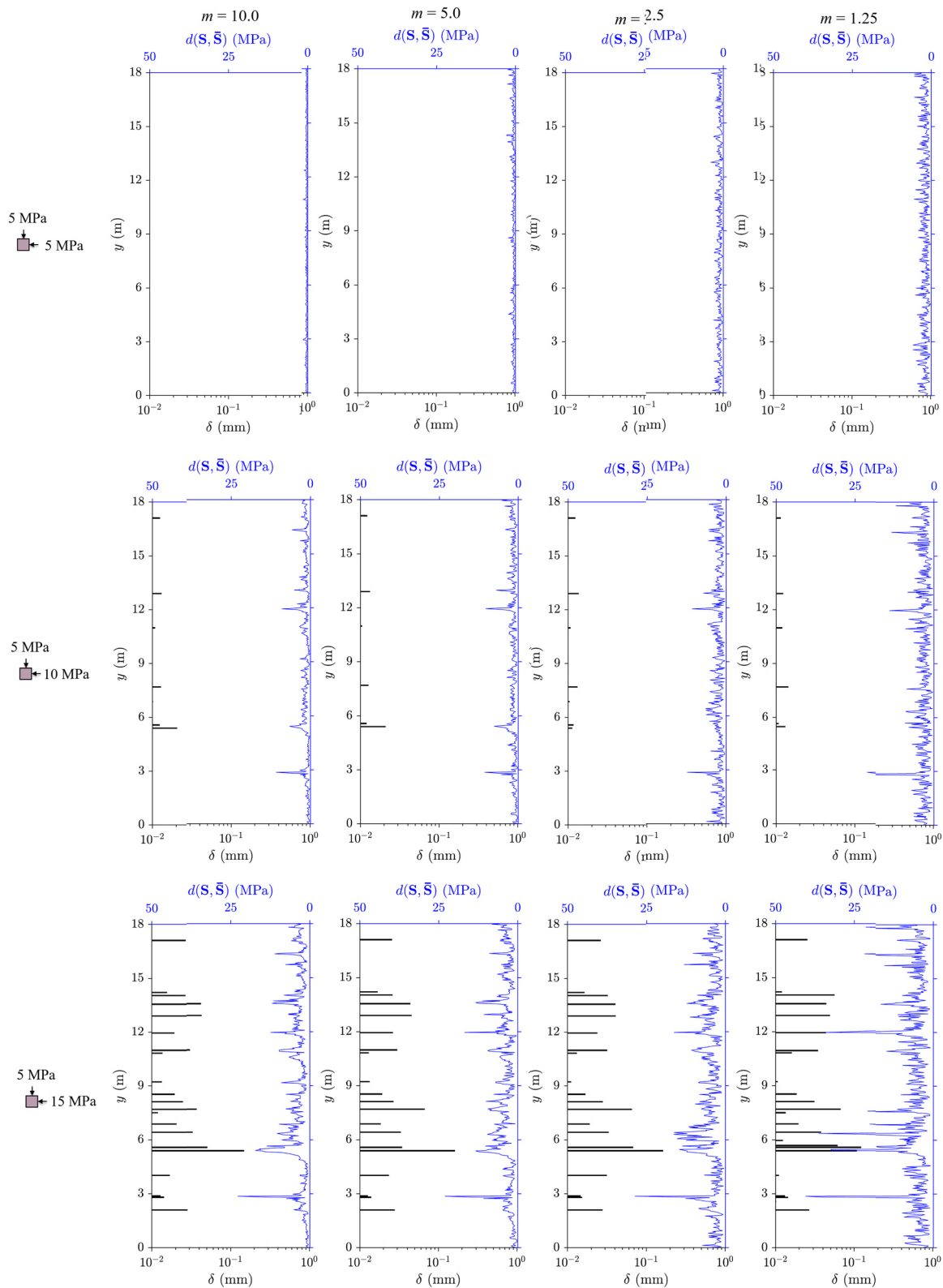
Fig. 7. The profiles of fracture shear displacement δ (in black) and local stress perturbation $d(\mathbf{S}, \bar{\mathbf{S}})$ (in blue) along a 1D scanline (x = 9 m, 0 ≤ y ≤ 18 m) across the heterogeneous fractured rock under different far-field stress ratio conditions. (For interpretation of the references to colour in this figure legend, the reader is referred to the web version of this article).

different degrees of material inhomogeneity and under different far-field stress ratio conditions. The probability density functions (PDFs) of δ and $d(\mathbf{S}, \bar{\mathbf{S}})$ of all these cases are further given in Fig. 6 (note that the PDF in Fig. 6b is based on a logarithmic x-axis but the total area of each

histogram equals to unity). Under the isotropic far-field stress loading, there is almost no shearing in the fracture network for all m cases (Figs. 5a and 6a). However, an increased amount of stress perturbation appears in the system as the rock becomes more heterogeneous (i.e. m
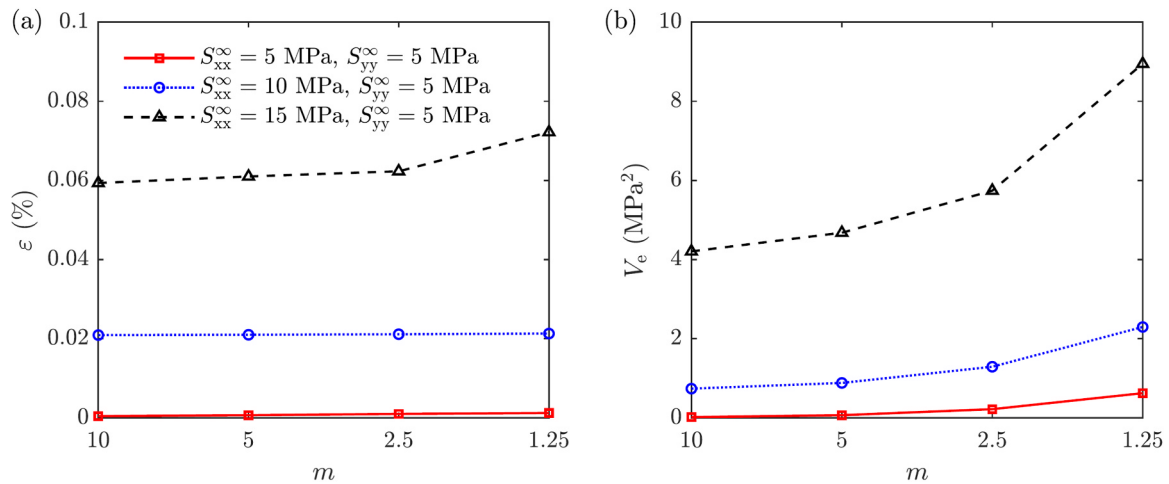
Fig. 8. (a) The total strain from frictional sliding ε and (b) effective variance of the stress field $V_e(\mathbf{S})$ in the heterogeneous fractured rock under different far-field stress ratio conditions.

decreases) (Figs. 5b and 6b). As the far-field stress ratio $S_{xx}^{\infty}/S_{yy}^{\infty}$ increases, significant shear displacement occurs (Figs. 5a and 6a) along some fractures that have good connectivity and are preferentially oriented for frictional sliding (Fig. 5a). Furthermore, for high $S_{xx}^{\infty}/S_{yy}^{\infty}$, considerable stress fluctuations emerge in the fractured rock, the degree of which is further intensified as m decreases (Figs. 5b and 6b). It is manifest that when $S_{xx}^{\infty}/S_{yy}^{\infty} = 3$, the stress perturbation in the case of $m = 1.0$ is much larger than those of other m cases.

We sample a 1D scanline ($x = 9$ m, $0 \leq y \leq 18$ m) across the domain and extract the shear displacement of fractures that intersect the scanline and local stress perturbation in the rock along this line. As shown in Fig. 7, under the isotropic far-field stress, there is no shearing along fractures, but certain stress perturbation still exists in the very heterogeneous rock (e.g. $m = 1.25$). As the far-field stress ratio increases, some of the fractures are reactivated for shearing and the stress field becomes strongly perturbed, which is further enhanced if the rock is more heterogeneous. It seems that the peaks of the stress perturbation profile correspond quite well to the locations of sheared fractures, while some minor mismatch is due to the effects of nearby fractures that are not sampled by the scanline. Other scanlines at different positions and with different orientations show similar results, but not presented here for the sake of brevity.

We evaluate the bulk shear behaviour of the fracture system using the total strain from frictional sliding ε, which is defined as the sum of the geometric moments (i.e. product of the average shear displacement and fracture length) of all fractures divided by the area of the domain.[39] We also characterise the overall stress variability using the effective variance of the entire stress tensor field $V_e(\mathbf{S})$. It can be seen that ε increases significantly as $S_{xx}^{\infty}/S_{yy}^{\infty}$ increases, the degree of which is further enhanced by a decreased m, especially when $S_{xx}^{\infty}/S_{yy}^{\infty} = 3$ (Fig. 8a). The system also exhibits larger stress dispersion with increasing $S_{xx}^{\infty}/S_{yy}^{\infty}$ and decreasing m (Fig. 8b). This is mainly due to the intensified fracture shearing driven by high differential stresses and non-uniform stress redistribution induced by material inhomogeneity. The latter factor seems to prevail over the former one in the highly heterogeneous rock, i.e. $m = 1.25$.

Fig. 9 shows the simulation results of shear displacement δ and local stress perturbation $d(\mathbf{S}, \bar{\mathbf{S}})$ in the fractured rock under far-field stresses of $S_{max}^{\infty} = 15.0$ MPa and $S_{min}^{\infty} = 5.0$ MPa that are imposed at different angles θ to the system (note that only the representative cases of $\theta = 10°$, $40°$ and $90°$ are shown). The PDFs of δ and $d(\mathbf{S}, \bar{\mathbf{S}})$ of these selected θ cases are given in Fig. 10. The scanline sampling results are

shown in Fig. 11. The total strain due to fracture shearing ε and the effective variance of the stress field $V_e(\mathbf{S})$ for all cases of $\theta = 0–170°$ are presented in Fig. 12.

It can be seen that the shear behaviour of fractures is strongly controlled by the orientation of far-field stresses relative to the orientation of fracture sets. Theoretically, the shear stress on a pre-existing fracture reaches its maximal when the angle between the S_{max}^{∞} direction and the fracture plane is $45°\text{-}\varphi/2$,[40] which is about $25°$ here given that the joint friction angle $\varphi \approx 40°$ (i.e. friction coefficient of 0.85). Thus, as shown in Fig. 9, in the case of $\theta = 10°$, the $50°$ fracture set exhibits higher shear displacement, while the other two sets (i.e. the $5°$ and $80°$ sets) are quite suppressed for shearing; in the case of $\theta = 40°$, the $5°$ fracture set is active in shear, while the other sets are less reactivated; in the case of $\theta = 90°$, both the $50°$ and $120°$ sets are at a favourable orientation for sliding. Figs. 10a and 11 further reveal that the cases of $\theta = 10°$ and $90°$ accommodate more shearing in the fracture system than the case of $\theta = 40°$. Thus, the total strain ε varies significantly with the orientation of far-field stresses, and reaches its maxima when $\theta \approx 90°$ and $170°$, and minima when $\theta \approx 40°$ and $120°$ (Fig. 12a). Furthermore, a decreased m tends to enhance the shearing of fractures (Figs. 9a, 10a, and 12a), especially when the far-field stresses are critically oriented to reactivate more than one set of fractures (e.g. when $\theta = 90°$, Fig. 12a).

The far-field stress orientation also has a significant influence on the local and global stress variability in the fractured rock. The stress field is highly perturbed when $\theta = 90°$, moderately perturbed when $\theta = 10°$, and much less perturbed when $\theta = 40°$ (Figs. 9b and 10b). It can be seen that the most perturbed region in the fractured rock is at the vicinity of fractures that are oriented in favour of shearing in each θ case (Fig. 9b), implying the important impact of fracture sliding and induced mechanical interactions on stress distribution. The relationship between fracture shearing and local stress perturbation can also be clearly seen from the displacement and stress profiles sampled from the scanline (Fig. 11). Additionally, an increased material inhomogeneity (i.e. decrease m) leads to pronounced local perturbations in the stress pattern in different θ cases (Figs. 9b and 10b). The effective variance of the stress field is also very sensitive to the far-field stress orientation, and exhibit three maxima and two minima (Fig. 12b), which is consistent with the variation of ε (Fig. 12a) and further confirms the correlation between fracture sliding and stress variability. Furthermore, an increased material inhomogeneity tends to considerably enlarge the overall stress dispersion (Fig. 12b).
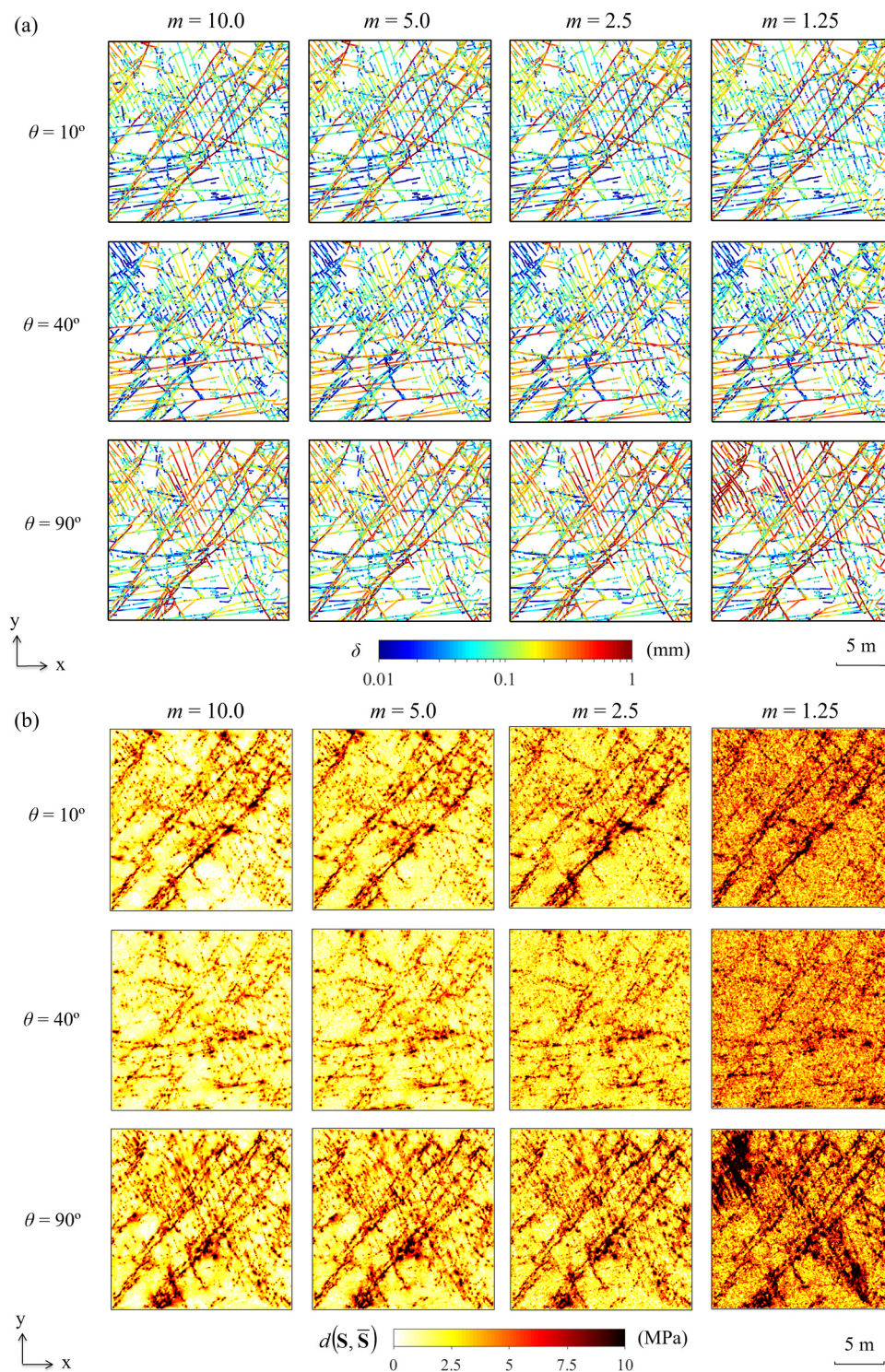
Fig. 9. Distributions of (a) shear displacement δ and (b) local stress perturbation $d(\mathbf{S}, \bar{\mathbf{S}})$ in the heterogeneous fractured rock under the far-field stress field of $S_{\max}^\infty$ = 15.0 MPa and $S_{\min}^\infty$ = 5.0 MPa applied at different angles of θ = 10°, 40° and 90°.

4. Discussion

The important influence of natural fractures on the stress distribution in geological media has been well recognised.[3,35] Extensive field measurements have revealed that significant stress jump and reorientation can occur in the vicinity of geological structures.[4,8,41–44] Previous numerical studies have also suggested that strong stress fluctuations can be created in the regions near active discontinuities

undergoing shear.[7,11,14,45] The observed correlation between the shearing along pre-existing fractures and the variability of local stresses in our work shows good consistency with these earlier studies. Furthermore, such a correlation is found to be strongly dependent on the far-field stress ratio and orientation. It is worth emphasising that we also elucidate the effect of inhomogeneous rock modulus on stress organisation, which may play a dominant role in highly heterogeneous rocks as a result of significant stress redistribution, i.e. the stiffer parts
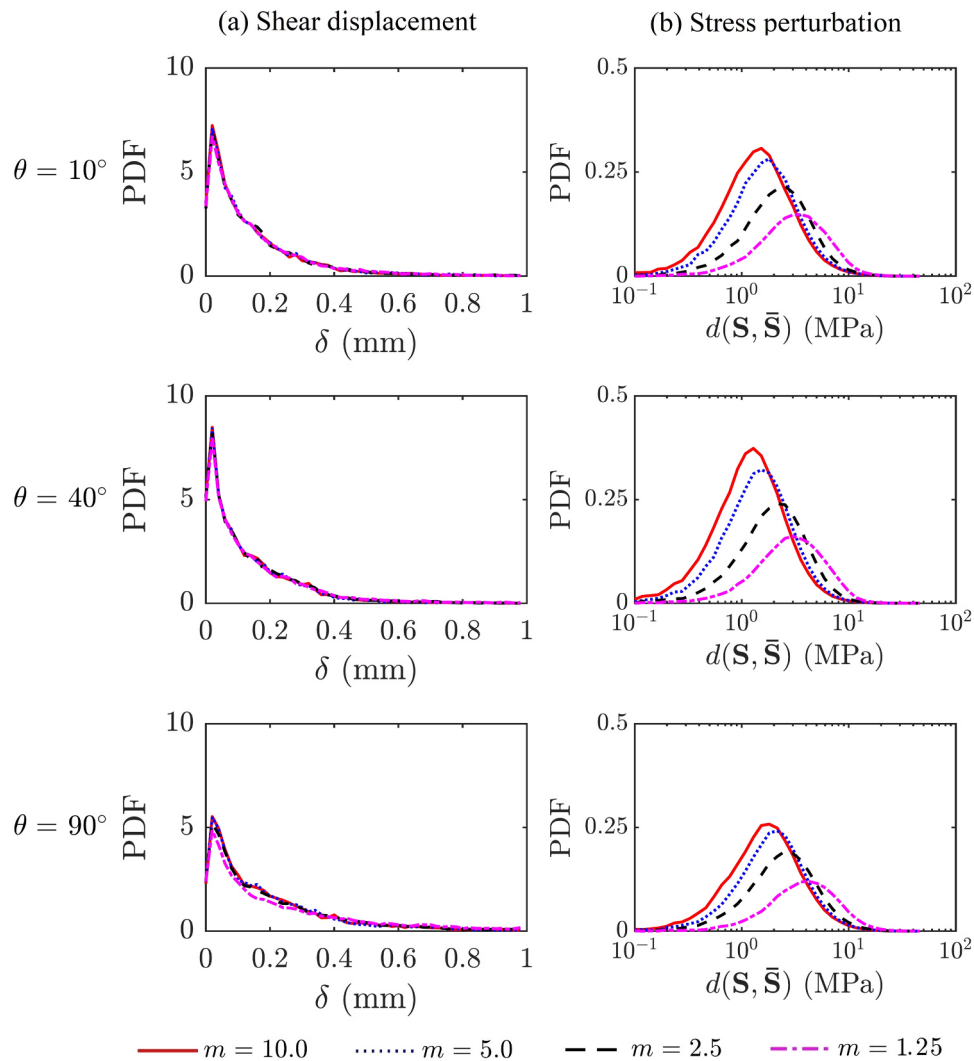
Fig. 10. Probability density functions (PDFs) of (a) shear displacement δ and (b) local stress perturbation $d(\mathbf{S}, \bar{\mathbf{S}})$ in the heterogenous fractured rock under the far-field stress field of $S_{max}^{\infty} = 15.0$ MPa and $S_{min}^{\infty} = 5.0$ MPa applied at different angles of $\theta = 10°$, $40°$ and $90°$.

of the rock sustain higher stresses than softer parts.[35] We schematically show in Fig. 13 that the stress variability in fractured rocks may be dominated by fractures or heterogeneous rocks (or both), depending on the conditions of material inhomogeneity, far-field stress ratio and fracture network. If the rock material is highly heterogeneous (i.e. m is small), stress variability is more dominated by the matrix when the far-field stress ratio is low; however, when fractures are reactivated for shearing driven by a high far-field stress ratio, the stress field becomes more affected by fractures. If the rock material is quite homogeneous (i.e. m is large), the system tends to be more dominated by fractures even under a relatively low far-field stress ratio. In between the matrix-dominated and fracture-dominated regimes, there is a transition regime where both factors are important. With an increase of the fracture network density and/or a decrease of the friction coefficient of fractures, the transition regime is expected to be more approaching to the bottom left of the diagram. This is because fractures tend to accommodate more slipping (as demonstrated from our previous work[9]) and thus dominate stress distribution.

Another finding of this paper is the interactive roles of far-field stress state, fracture distribution and material inhomogeneity in the development of variable local stresses in fractured rocks. It is commonly known that when the far-field stresses are loaded with a high stress ratio and at a critical orientation to the fracture system, some of the fractures are highly stimulated for shearing, which leads to stress concentration at their tips/intersections and stress reorientation in their proximity. In this research, we further observe that the inhomogeneous nature of rock modulus can result in more unevenly loaded normal/shear forces along these fractures, while the sliding of fractures may reinforce the effect of material inhomogeneity by generating more variable boundary stresses around matrix blocks. This may explain the variation of total strain and stress dispersion in the anisotropic fracture system with the rotation of far-field stresses and the homogeneity condition of rock materials, as observed in Fig. 12.

5. Conclusions

To conclude, we studied the variability of stress field in heterogeneous fractured rocks under different far-field stress conditions. A fracture network based on a sandstone outcrop was used and the inhomogeneous nature of rock was modelled according to the Weibull distribution of its Young's modulus. Geomechanical modelling based on a hybrid finite-discrete element method was conducted to calculate the local stress field in the fractured rock under far-field stresses loaded at different stress ratios and orientations. The derived stress data were
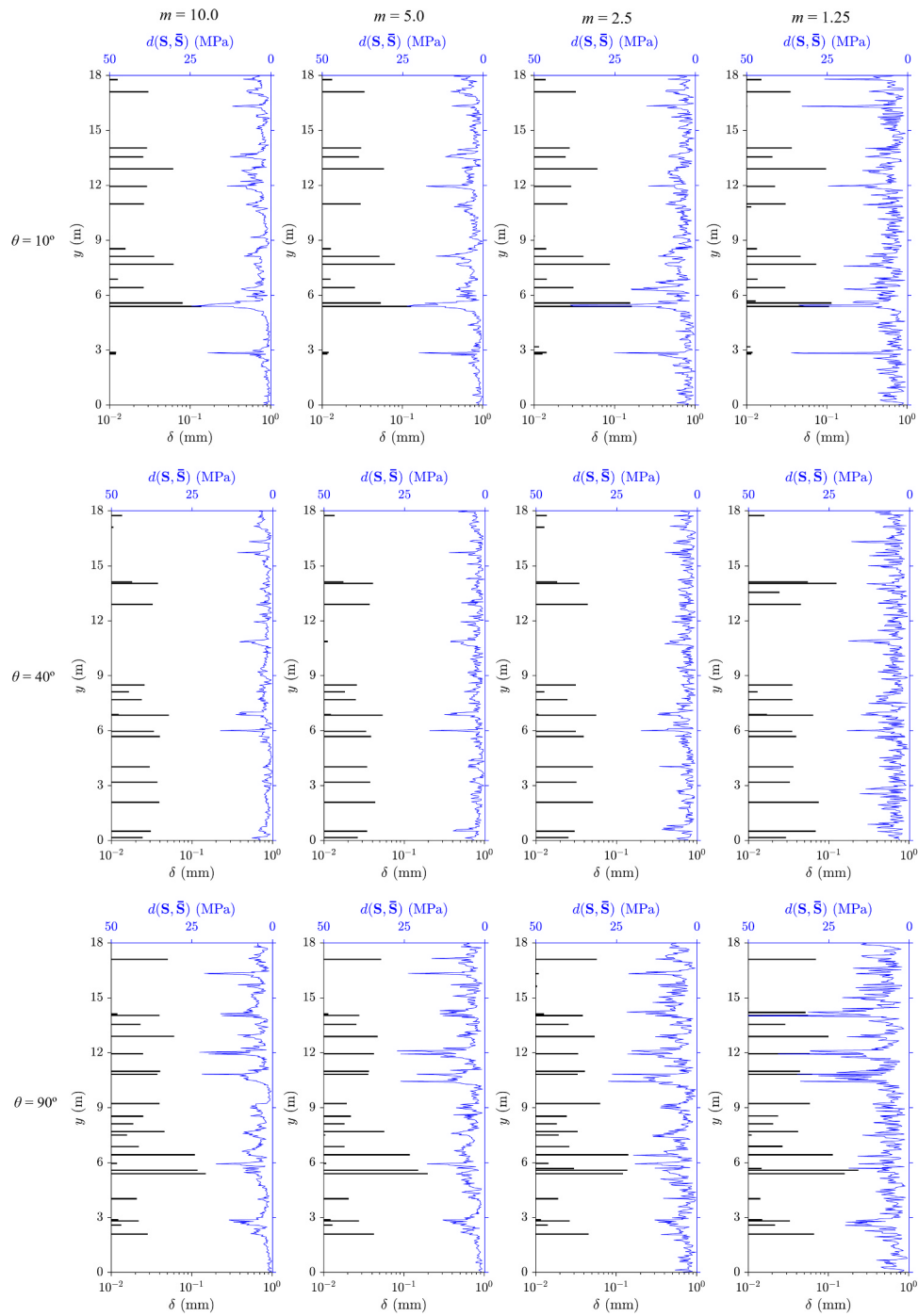
Fig. 11. The distributions of fracture shear displacement δ (in black) and local stress perturbation $d(\mathbf{S}, \bar{\mathbf{S}})$ (in blue) along a 1D sampling line (x = 9 m, 0 ≤ y ≤ 18 m) through the heterogeneous fractured rock. (For interpretation of the references to colour in this figure legend, the reader is referred to the web version of this article).

further processed using a novel tensor-based approach that fully honours the tensorial nature of stresses. The local stress perturbation was quantified using the Euclidean distance of the local stress tensor to the mean stress tensor, and the overall dispersion was evaluated using the effective variance of the entire stress field. It was found that local stress field is significantly perturbed when the far-field stresses are imposed with a high stress ratio and at a critical orientation in favour of intense shearing along fracture walls. Furthermore, the local stress field

exhibits stronger disturbance as the rock becomes more heterogeneous. This paper provided valuable insights into the interactive roles of far-field stress state, fracture network and material inhomogeneity in causing stress variability in geological media, and whether the stress field is dominated by fractures or matrix depends on these three factors. The results may have important implications for understanding the stress state of the Earth's crust for geoengineering applications.
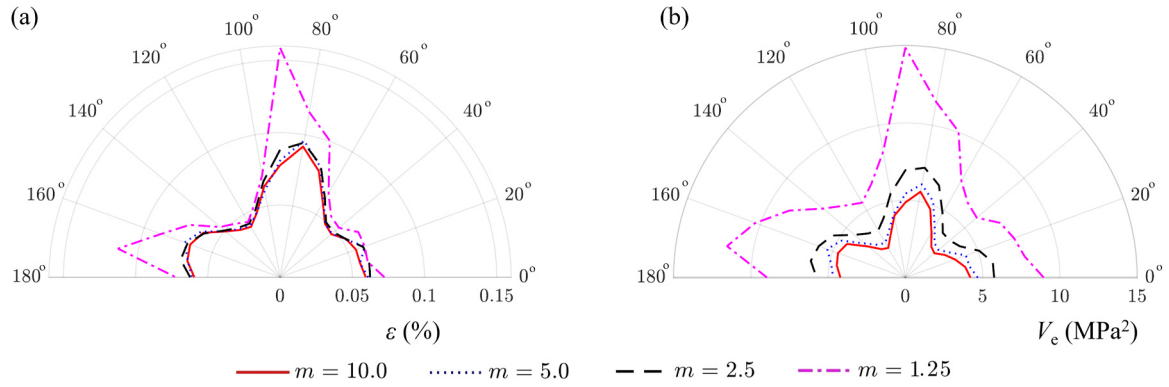
Fig. 12. Rose diagram showing the variation of (a) total strain from frictional sliding ε and (b) effective variance of the stress field $V_e(\mathbf{S})$ in the heterogeneous fractured rock with respect to the orientation θ of the far-field stress field of $S_{\max}^{\infty} = 15.0$ MPa and $S_{\min}^{\infty} = 5.0$ MPa.
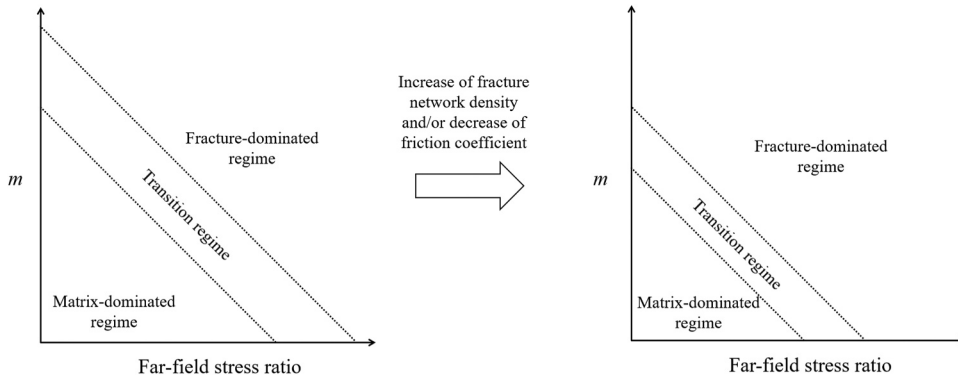

Fig. 13. Schematic illustration of the different regimes where stress variability in fractured rocks is dominated by heterogenous rock matrix or fractures, which depends on the material homogeneity index m, the far-field stress condition and the fracture network properties. Note that the actual boundaries between different regimes do not necessarily have to be linear.

Appendix A. Tensor-based stress variability characterisation

In a 2D stress tensor field $\mathbf{S}$, which consists of n stress measurements, the ith stress tensor $\mathbf{S}_i$ is written as:

$$\mathbf{S}_i = \begin{bmatrix} S_{xx,i} & S_{xy,i} \\ \text{symmetric} & S_{yy,i} \end{bmatrix}. \tag{A.1}$$

The mean tensor of the entire stress field is calculated as[36]:

$$\bar{\mathbf{S}} = \frac{1}{n}\sum_{i=1}^{n}\mathbf{S}_i = \frac{1}{n}\begin{bmatrix} \sum_{i=1}^{n} S_{xx,i} & \sum_{i=1}^{n} S_{xy,i} \\ \text{symmetric} & \sum_{i=1}^{n} S_{yy,i} \end{bmatrix}. \tag{A.2}$$

Since the mean stress tensor in a fractured rock approximates to the far-field stress tensor,[9,46] we can use the Euclidean distance between a local stress tensor $\mathbf{S}_i$ and the mean stress tensor $\bar{\mathbf{S}}$, i.e.

$$d(\mathbf{S}_i, \bar{\mathbf{S}}) = \|\mathbf{S}_i - \bar{\mathbf{S}}\|_F, \tag{A.3}$$

as an indicator of local stress perturbation to the far-field stress state, where $\|\cdot\|_F$ denotes the Frobenius norm (also known as the Euclidean norm or Hilbert-Schmidt norm).[47] In a purely uniform stress field, $d(\mathbf{S}, \bar{\mathbf{S}})$ is zero throughout, while for a heterogeneous stress field, $d(\mathbf{S}, \bar{\mathbf{S}})$ can vary significantly from point to point in the system.

In addition, the variability of stress tensor can be adequately represented by the variability of its distinct tensor components in a multivariate statistics manner.[26] Thus, the overall variability of a stress field can be described by its effective variance – a widely used concept in the field of multivariate statistics for group dispersion measure.[48] For a stress tensor $\mathbf{S}_i$, its distinct components form a stress vector $\mathbf{s}_i$ as:

$$\mathbf{s}_i = \text{vech}(\mathbf{S}_i) = [S_{xx,i} \quad S_{yx,i} \quad S_{yy,i}]^T = [S_{xx,i} \quad S_{xy,i} \quad S_{yy,i}]^T, \tag{A.4}$$

where vech($\cdot$) is the half-vectorisation function that stacks only the lower triangular (i.e. on and below the diagonal) columns of a tensor into a column vector containing only the distinct components. The effective variance is then calculated as[49]:

$$V_e(\mathbf{S}) = \sqrt[\frac{1}{2}p(p+1)]{\det(\boldsymbol{\Omega})}, \tag{A.5}$$

where p is the dimension of the stress tensor ($p = 2$ here), and $\boldsymbol{\Omega}$ is the covariance matrix of the stress vector field $\mathbf{s}$:

$$\boldsymbol{\Omega} = \text{cov}(\mathbf{s}, \mathbf{s}) = \frac{1}{n}\sum_{i=1}^{n}[(\mathbf{s}_i - \bar{\mathbf{s}})\cdot(\mathbf{s}_i - \bar{\mathbf{s}})^T], \tag{A.6}$$

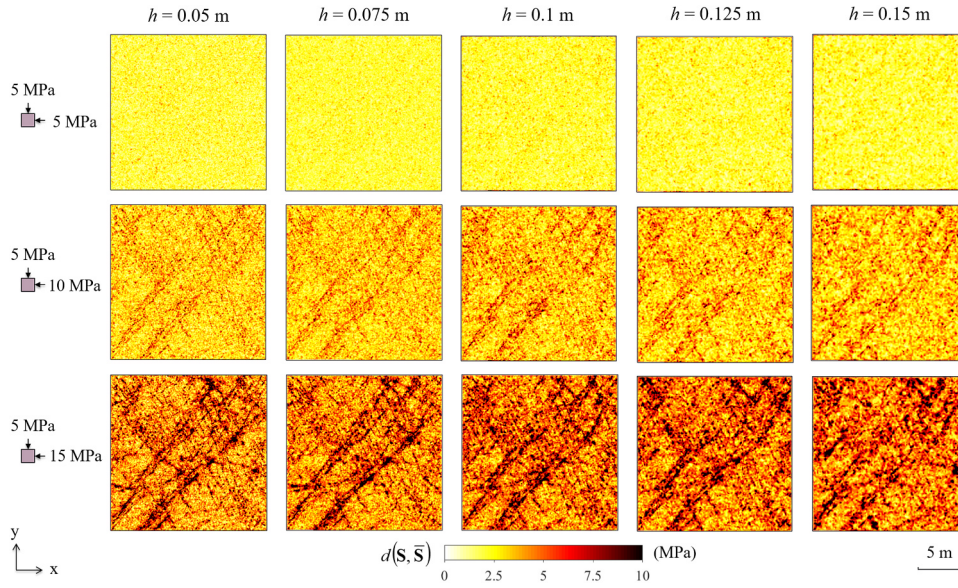where $\bar{\mathbf{s}}$ is the mean stress vector:

Fig. A.1. Mesh sensitivity analysis of simulated local stress perturbation field $d(\mathbf{S}, \bar{\mathbf{S}})$ in the heterogeneous fractured rock with a homogeneity index of $m = 1.25$ under different far-field stress ratios Here, h denotes the average element size.
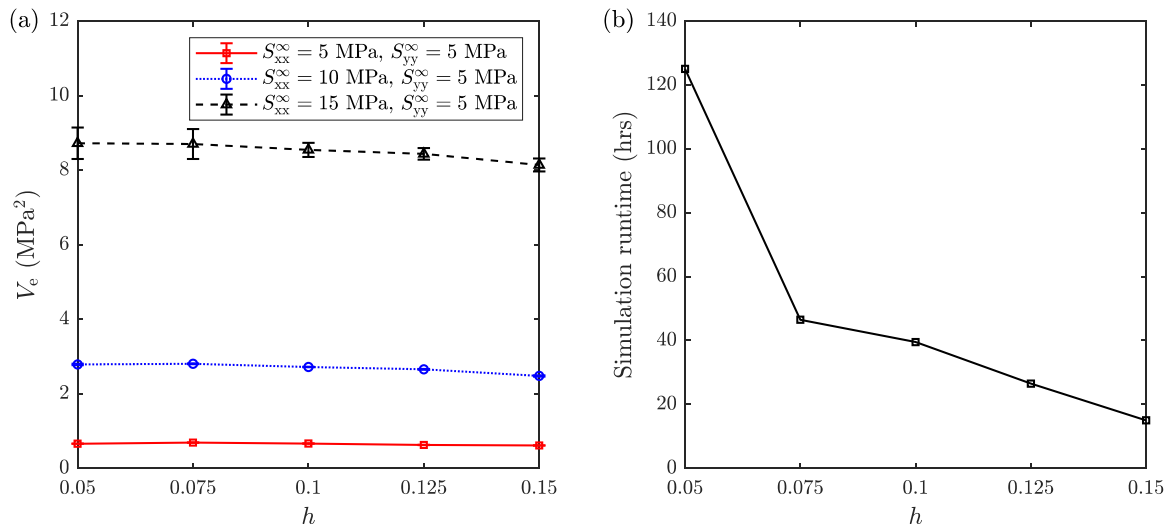

Fig. A.2. (a) Mesh sensitivity analysis of calculated effective variance of the stress field $V_e(\mathbf{S})$ in the heterogeneous fractured rock with a homogeneity index of $m = 1.25$ under different far-field stress ratios. Here, h denotes the average element size and the error bars denote the standard deviation of the results of ten material heterogeneity realisations. (b) Variation of simulation runtime with respect to the average element size. Note that the runtime is based on a desktop computer equipped with an Intel(R) Xeon(R) CPU E3–1284L v4 @2.90 GHz.

$$\bar{\mathbf{s}} = \frac{1}{n} \sum_{i=1}^{n} \mathbf{s}_i. \tag{A.7}$$

The effective variance gives a scalar-valued measure of how spread out a stress tensor group is with respect to their mean, and it has the same unit as the variance of stress components, i.e. square of the unit of stress. We therefore use the effective variance to measure the bulk stress variability in the heterogeneous fractured rocks. The larger the effective variance is, the more dispersed the stress field is.

Appendix B. Mesh sensitivity analysis

We have conducted a mesh sensitivity analysis of the numerical model for calculating stress variability in heterogeneous fractured rocks, in which a range of average element sizes $h = 0.05, 0.075, 0.1, 0.125$ and 0.15 m, covering from fine to coarse mesh configurations, have been explored. We focus on the very heterogeneous rock with a homogeneity index of $m = 1.25$, which is considered to be more sensitive to mesh size compared to other relatively homogeneous rocks with larger m values. We also generate ten realisations of Weibull distribution of rock moduli to examine the potential randomness effect (i.e. modulus values are randomly assigned to model elements). As shown in Fig. A.1, with the increase of model resolution (i.e. decrease of h), the local stress perturbation can be captured in more detail, especially in the vicinity of fractures. We also compare the results of the effective variance V_e of the entire stress field derived from the models of different element sizes (Fig. A.2a). It can be seen that with the

increase of model resolution (i.e. decrease of h), V_e exhibits a slight increase, suggesting that more stress variability is captured in refined models. However, the computational runtime increases significantly with the model refinement (Fig. A.2b). Thus, an average element size of 0.075 m is adopted in the paper to achieve computational efficiency without sacrificing model accuracy.

References

1. Zang A, Stephansson O. *Stress Field of the Earth's Crust.* Berlin: Springer; 2010.
2. Zoback ML. First- and second-order patterns of stress in the lithosphere: the world stress map project. *J Geophys Res.* 1992;97(B8):11703–11728. https://doi.org/10.1029/92JB00132.
3. Hudson JA, Cooling CM. In situ rock stresses and their measurement in the U.K.—Part I. The current state of knowledge. *Int J Rock Mech Min Sci Geomech Abstr.* 1988;25(6):363–370. https://doi.org/10.1016/0148-9062(88)90976-X.
4. Sahara DP, Schoenball M, Kohl T, Müller BIR. Impact of fracture networks on borehole breakout heterogeneities in crystalline rock. *Int. J. Rock Mech. Min. Sci.* 2014;71:301–309. https://doi.org/10.1016/j.ijrmms.2014.07.001.
5. Valley BC. *The Relation between Natural Fracturing and Stress Heterogeneities in Deep-Seated Crystalline Rocks at Soultz-Sous- Forêts (France) (Ph.D. thesis).* Zürich: Swiss Federal Institute of Technology Zürich; 2007.
6. Yale DP. Fault and stress magnitude controls on variations in the orientation of in situ stress. In: Ameen M, ed. London: Geological Society London, Special Publications; 2003:55–64. https://doi.org/10.1144/GSL.SP.2003.209.01.06. Fracture and In-Situ Stress Characterization of Hydrocarbon Reservoirs; 209.
7. Stephansson O, Ljunggren C, Jing L. Stress measurements and tectonic implications for Fennoscandia. *Tectonophysics.* 1991;189(1–4):317–322. https://doi.org/10.1016/0040-1951(91)90504-L.
8. Chang C, Jo Y. Heterogeneous in situ stress magnitudes due to the presence of weak natural discontinuities in granitic rocks. *Tectonophysics.* 2015;664:83–97. https://doi.org/10.1016/j.tecto.2015.08.044.
9. Lei Q, Gao K. Correlation between fracture network properties and stress variability in geological media. *Geophys ResLett.* 2018;45(9):3994–4006. https://doi.org/10.1002/2018GL077548.
10. Rutqvist J, Leung C, Hoch A, Wang Y, Wang Z. Linked multicontinuum and crack tensor approach for modeling of coupled geomechanics, fluid flow and transport in fractured rock. *J Rock Mech Geotech Eng.* 2013;5(1):18–31. https://doi.org/10.1016/j.jrmge.2012.08.001.
11. Figueiredo B, Tsang C-F, Rutqvist J, Niemi A. A study of changes in deep fractured rock permeability due to coupled hydro-mechanical effects. *Int J Rock Mech Min Sci.* 2015;79:70–85. https://doi.org/10.1016/j.ijrmms.2015.08.011.
12. Min K-B, Jing L. Numerical determination of the equivalent elastic compliance tensor for fractured rock masses using the distinct element method. *Int J Rock Mech Min Sci.* 2003;40(6):795–816. https://doi.org/10.1016/S1365-1609(03)00038-8.
13. Mas Ivars D, Pierce ME, Darcel C, et al. The synthetic rock mass approach for jointed rock mass modelling. *Int J Rock Mech Min Sci.* 2011;48(2):219–244. https://doi.org/10.1016/j.ijrmms.2010.11.014.
14. Lei Q, Latham J-P, Xiang J, Tsang C-F, Lang P, Guo L. Effects of geomechanical changes on the validity of a discrete fracture network representation of a realistic two-dimensional fractured rock. *Int J Rock Mech Min Sci.* 2014;70:507–523. https://doi.org/10.1016/j.ijrmms.2014.06.001.
15. Lei Q, Latham J-P, Tsang C-F. The use of discrete fracture networks for modelling coupled geomechanical and hydrological behaviour of fractured rocks. *Comput Geotech.* 2017;85:151–176. https://doi.org/10.1016/j.compgeo.2016.12.024.
16. Tang CA. Numerical simulation of progressive rock failure and associated seismicity. *Int J Rock Mech Min Sci.* 1997;34(2):249–261. https://doi.org/10.1016/S0148-9062(96)00039-3.
17. Tang CA, Liu H, Lee PKK, Tsui Y, Tham LG. Numerical studies of the influence of microstructure on rock failure in uniaxial compression — Part I: effect of heterogeneity. *Int J Rock Mech Min Sci.* 2000;37(4):555–569. https://doi.org/10.1016/S1365-1609(99)00121-5.
18. Tang CA, Liang ZZ, Zhang YB, et al. Fracture spacing in layered materials: a new explanation based on two-dimensional failure process modeling. *Am J Sci.* 2008;308(1):49–72. https://doi.org/10.2475/01.2008.02.
19. Ma GW, Wang XJ, Ren F. Numerical simulation of compressive failure of heterogeneous rock-like materials using SPH method. *Int J Rock Mech Min Sci.* 2011;48(3):353–363. https://doi.org/10.1016/j.ijrmms.2011.02.001.
20. Fang Z, Harrison JP. Development of a local degradation approach to the modelling of brittle fracture in heterogeneous rocks. *Int J Rock Mech Min Sci.* 2002;39(4):443–457. https://doi.org/10.1016/S1365-1609(02)00035-7.
21. Yuan SC, Harrison JP. A review of the state of the art in modelling progressive mechanical breakdown and associated fluid flow in intact heterogeneous rocks. *Int J Rock Mech Min Sci.* 2006;43(7):1001–1022. https://doi.org/10.1016/j.ijrmms.2006.03.004.
22. Chen W, Konietzky H. Simulation of heterogeneity, creep, damage and lifetime for loaded brittle rocks. *Tectonophysics.* 2014;633(1):164–175. https://doi.org/10.1016/j.tecto.2014.06.033.
23. Farahmand K, Vazaios I, Diederichs MS, Vlachopoulos N. Investigating the scale-dependency of the geometrical and mechanical properties of a moderately jointed rock using a synthetic rock mass (SRM) approach. *Comput Geotech.*
24. Ghazvinian E, Diederichs MS, Quey R. 3D random Voronoi grain-based models for simulation of brittle rock damage and fabric-guided micro-fracturing. *J Rock Mech Geotech Eng.* 2014;6:506–521. https://doi.org/10.1016/j.jrmge.2014.09.001.
25. Weibull W. A statistical distribution function of wide applicability. *J Appl Mech.* 1951;18:293–297.
26. Gao K, Harrison JP. Multivariate distribution model for stress variability characterisation. *Int J Rock Mech Min Sci.* 2018;102:144–154. https://doi.org/10.1016/j.ijrmms.2018.01.004.
27. Odling NE. Scaling and connectivity of joint systems in sandstones from western Norway. *J Struct Geol.* 1997;19(10):1257–1271. https://doi.org/10.1016/S0191-8141(97)00041-2.
28. Munjiza A. *The Combined Finite-Discrete Element Method.* London: Wiley; 2004.
29. Lei Q, Latham J-P, Xiang J. Implementation of an empirical joint constitutive model into finite-discrete element analysis of the geomechanical behaviour of fractured rocks. *Rock Mech Rock Eng.* 2016;49(12):4799–4816. https://doi.org/10.1007/s00603-016-1064-3.
30. Pollard DD, Segall P. Theoretical displacements and stresses near fractures in rock: with applications to faults, joints, veins, dikes, and solution surfaces. In: Atkinson BK, ed. *Fracture Mechanics of Rock.* San Diego: Academic Press; 1987:277–349.
31. Lama RD, Vutukuri VS. Handbook on Mechanical Properties of Rocks: Testing Techniques and Results (Vol. 2). Clausthal: Trans. Tech. Publications; 1978.
32. Byerlee J. Friction of rocks. *Pure Appl Geophys.* 1978;116(4–5):615–626. https://doi.org/10.1007/BF00876528.
33. Barton N, Choubey V. The shear strength of rock joints in theory and practice. *Rock Mech.* 1977;10(1–2):1–54. https://doi.org/10.1007/BF01261801.
34. Hudson JA, Fairhurst C. Tensile strength, Weibull's theory and a general statistical approach to rock failure. In: Te'eni M, ed. The Proceedings of International Conference on Structure, Solid Mechanics and Engineering Design in Civil Engineering Matrials. Southampton; 1969:901-914.
35. Amadei B, Stephansson O. *Rock Stress and its Measurement.* London: Springer; 1997.
36. Gao K, Harrison JP. Mean and dispersion of stress tensors using Euclidean and Riemannian approaches. *Int J Rock Mech Min Sci.* 2016;85:165–173. https://doi.org/10.1016/j.ijrmms.2016.03.019.
37. Gao K, Harrison JP. Generation of random stress tensors. *Int J Rock Mech Min Sci.* 2017;94:18–26. https://doi.org/10.1016/j.ijrmms.2016.12.011.
38. Gao K, Harrison JP. Re-examination of the in situ stress measurements on the 240 level of the AECL's URL using tensor-based approaches. *Rock Mech Rock Eng.* 2018. https://doi.org/10.1007/s00603-018-1530-1.
39. Marrett R, Allmendinger RW. Estimates of strain due to brittle faulting: sampling of fault populations. *J Struct Geol.* 1991;13(6):735–738. https://doi.org/10.1016/0191-8141(91)90034-G.
40. Zoback MD. *Reservoir Geomechanics.* Cambridge: Cambridge University Press; 2007https://doi.org/10.1017/CBO9780511586477.
41. Martin CD, Chandler NA. Stress heterogeneity and geological structures. *Int J Rock Mech Min Sci.* 1993;30(7):993–999. https://doi.org/10.1016/0148-9062(93)90059-M.
42. Bruno MS, Winterstein DF. Some influences of stratigraphy and structure on reservoir stress orientation. in: *Proceedings of the SPE Annual Technical Conference and Exhibition.* Washington DC: Society of Petroleum Engineers. 1992:875–883. ⟨https://www.doi.org/10.2118/24746-MS⟩.
43. Lin W, Yeh EC, Hung JH, Haimson B, Hirono T. Localized rotation of principal stress around faults and fractures determined from borehole breakouts in hole B of the Taiwan Chelungpu-fault Drilling Project (TCDP). *Tectonophysics.* 2010;482(1–4):82–91. https://doi.org/10.1016/j.tecto.2009.06.020.
44. Barton CA, Zoback MD. Stress perturbations associated with active faults penetrated by boreholes: possible evidence for near-complete stress drop and a new technique for stress magnitude measurement. *J Geophys Res Solid Earth.* 1994;99(B5):9373–9390. https://doi.org/10.1029/93JB03359.
45. Su S, Stephansson O. Effect of a fault on in situ stresses studied by the distinct element method. *Int J Rock Mech Min Sci.* 1999;36(8):1051–1056. https://doi.org/10.1016/S1365-1609(99)00119-7.
46. Gao K, Harrison JP, Lei Q, Latham J-P. Investigating the relationship between far-field stress and local values of the stress tensor. *Procedia Eng.* 2017;191:536–542. https://doi.org/10.1016/j.proeng.2017.05.215.
47. Gentle JE. *Matrix Algebra: Theory, Computations, and Applications in Statistics.* New York, NY: Springer; 2007https://doi.org/10.1007/978-0-387-70873-7.
48. Peña D, Rodríguez J. Descriptive measures of multivariate scatter and linear dependence. *J Multivar Anal.* 2003;85(2):361–374. https://doi.org/10.1016/S0047-259X(02)00061-1.
49. Gao K, Lei Q. Influence of boundary constraints on stress heterogeneity modelling. *Comput Geotech.* 2018;99(February):130–136. https://doi.org/10.1016/j.compgeo.2018.03.003.